PAPER

Check for updates

Adsorption of mercury(II) with an Fe_3O_4 magnetic polypyrrole–graphene oxide nanocomposite

Chao Zhou, He Zhu, Qin Wang, Junxiu Wang, Juan Cheng, Yongfu Guo, [ID] *
Xiaoji Zhou and Renbi Bai*

To enhance the ability to remove mercury(II) from aqueous media, an Fe_3O_4 magnetic nanocomposite (PPy–GO) composed of polypyrrole (PPy) and graphene oxide (GO) was synthesized *in situ* and characterized *via* scanning electron microscopy (SEM), energy dispersive X-ray spectroscopy (EDX), transmission electron microscopy (TEM), X-ray photoelectron spectrometry (XPS), X-ray diffraction (XRD), Fourier transform-infrared spectroscopy (FT-IR), zeta potential analysis, vibrating sample magnetometer (VSM) and the Brunauer−Emmett−Teller (BET) method. The performance of the magnetic PPy–GO for adsorbing mercury(II) from water along with the effects of solution pH, adsorbent dosage, coexisting ions, reaction time and temperature were studied in detail. The adsorption kinetics, isotherms and thermodynamics were investigated in detail to gain insights into the adsorption process. The results show that the BET surface area of the magnetic PPy–GO reached $1737.6 \text{ m}^2 \text{ g}^{-1}$. The Langmuir capacity of the magnetic PPy–GO for mercury(II) adsorption was 400.0 mg g^{-1} at 300 K and pH 7 ± 0.1. After adsorption, the magnetic PPy–GO nanocomposite could be efficiently separated from water *via* a magnetic field. The adsorption process was endothermic and spontaneous and occurred in accord with the Langmuir and pseudo-second-order models. The overall adsorption of mercury(II) not only involved chemisorption, but was also partially governed by intra-particle diffusion. Data from the preliminary application of magnetic PPy–GO to remove heavy metals from real electroplating effluent indicated a high removal efficiency of over 99% for mercury(II). Finally, a possible adsorption mechanism was discussed. All data showed that the magnetic PPy–GO material is a promising adsorbent to remove mercury(II) from aqueous media.

1. Introduction

The pollution of heavy metals has become more and more serious due to the flourishing development of community economy, industry and agriculture.[1] Mercury, cadmium, nickel, copper, lead, zinc and chromium are the most common heavy metals contributing to serious pollution.[2,3] Among these trace heavy metals, mercury(II) has drawn much attention because of its adverse impact on human beings and the natural environment. After wastewater containing mercury is discharged into natural water, the accumulation of mercuric compounds in the bodies of humans and animals occurs, resulting in adverse effects.[4] In many countries, mercury is considered as a serious and hazardous pollutant. The maximum acceptable content of mercury for human beings recommended by the WHO is $6 \text{ }\mu\text{g L}^{-1}$ in drinking water.[5]

It is very important to separate mercury from aqueous media before they are released into water bodies. Many methods can be employed to separate mercury from aqueous media,

including physical, chemical and biological methods.[6] Among these technologies, adsorption is often used to remove heavy metals owing to its higher efficiency and wider adaptability.[7,8]

Graphene oxide (GO), a derivative of graphene with an extremely large BET surface area, contains plentiful oxygen-containing functional groups with negative charges in its structure, including hydroxyl, epoxide and carboxyl groups.[9,10] These hydrophilic oxygen-containing functional groups make GO easily dissolve to form homogeneous suspensions under ultrasonic exfoliation.[11] These advantages also give GO the potential to separate heavy metal ions from aqueous media. Yang *et al.* employed GO to remove Cr(III) from water.[12] Tan *et al.* also reported the removal of Ni(II) and Cd(II) from aqueous solutions using GO materials.[13]

Nevertheless, it is difficult to separate GO from aqueous media after adsorption due to its low specific weight and small particle size. Magnetic separation provides a promising technique for the separation of GO materials due to its simplicity,[14] high efficiency and rapid speed compared to filtration and centrifugation.[1,15,16]

For instance, Wang *et al.* applied magnetic chitosan/GO to adsorb Pb(II) and obtained a maximum adsorption capacity of 79 mg g^{-1} (BET surface area $= 392.5 \text{ m}^2 \text{ g}^{-1}$, pH $= 5$);[17] Cui *et al.*

Center for Separation and Purification Materials & Technologies, Suzhou University of Science and Technology, Suzhou 215009, P. R. China. E-mail: yongfuguo@163.com; Tel: +86-512-68092987

used xanthate-functionalized magnetic GO to remove mercury(II) and reached a capacity of 118.6 mg g^{-1} (BET surface area = 30.1 m^2 g^{-1}, pH = 7).[18]

However, the adsorption capacity of GO for heavy metals in water is still not high enough due to its low BET value when it is used as the basic adsorption material.[19]

Polypyrrole (PPy), one of the most common conductive polymers, has some unique characteristics such as high conductivity, good environmental stability, non-toxicity, low cost and ease of preparing, and PPy has been widely used in batteries, sensors, supercapacitors and microwave shielding devices.

Researchers have found that positive charges exist in the PPy polymer due to the presence of nitrogen atoms. Moreover, PPy polymer can participate in ion exchange with anions in aqueous solution owing to its high surface energy, making it an ideal adsorbent material. Based on these properties, researchers have begun to study the application of PPy polymer to the adsorption of heavy metal ions in water.[20]

Shafiabadi *et al.* employed polypyrrole (PPy)/SBA-15 to remove mercury(II) and realized an adsorption capacity of 200 mg g^{-1} (BET surface area = 97.6 m^2 g^{-1}, pH = 8).[21] Chávez-Guajardo *et al.* used a polypyrrole/maghemite magnetic nanocomposite to remove Cr(VI) and obtained a capacity of 208.8 mg g^{-1} (BET surface area = 30 m^2 g^{-1}, pH = 2).[22]

However, it is easy for PPy polymer to agglomerate in water due to the existence of Π* in the main chain of the PPy polymer. In addition, the small BET value and poor dispersion in water of PPy polymer result in a low adsorption capacity for heavy metals. At present, the practical uses of adsorption devices in water treatment usually involve a fixed bed/column/tower and employ fillers with large density and large size. Thus, it is difficult to apply PPy polymer and GO in practical engineering owing to their small sizes and low densities.

Based on the above considerations, the combination of PPy polymer and GO with the addition of magnetic nanoparticles should not only enhance the physical and chemical properties of PPy and GO, but also increase their density and size. At the same time, this method can also remarkably increase the BET surface areas of the two nanomaterials and improve their dispersion in water so as to enhance the adsorption capacity for heavy metals. This is expected to allow the application of PPy polymer and GO materials in a fixed bed/column/tower in practical engineering activities.

Therefore, a magnetic polypyrrole–graphene oxide nanocomposite (PPy–GO) was chemically synthesized with pyrrole monomer and GO *in situ via* the doping of magnetic nanoparticles. The as-prepared magnetic PPy–GO nanocomposite was employed to remove mercury(II) from aqueous solution. Batch adsorption experiments were carried out to investigate in detail the performance of the magnetic PPy–GO for the removal of mercury(II). The study is summarized by the following steps: (a) produce the magnetic PPy–GO adsorbent with large BET surface area; (b) investigate influence of solution pH, adsorbent dosage, equilibrium time, adsorption temperature and coexisting ions; (c) investigate the adaptability of several adsorption models; (d) discuss the probable adsorption mechanism for mercury(II) onto the magnetic PPy–GO.

2. Experimental

2.1 Materials and reagents

Pyrrole monomer (Py, 98%), graphite (750–850 mesh), iron sulfate heptahydrate (FeSO$_4$·7H$_2$O) and hydrogen peroxide (H$_2$O$_2$) were obtained from Sinopharm Chemical Reagent Co., Ltd (Shanghai, China). Potassium permanganate (KMnO$_4$), mercury(II) chloride (HgCl$_2$), sodium nitrate (NaNO$_3$), iron chloride hexahydrate (FeCl$_3$·6H$_2$O), sulfuric acid (H$_2$SO$_4$), nitric acid (HNO$_3$), hydrochloric acid (HCl), potassium peroxydisulfate (K$_2$S$_2$O$_8$) and phosphorus pentoxide (P$_2$O$_5$) were provided by Aladdin Chemical. The chemicals used were all of analytical grade.

2.2 Preparation of materials

2.2.1 Preparation of GO. Natural graphite was used as the raw material to prepare graphite oxide *via* a modified Hummers' method.[23,24] First, natural graphite (2.0 g), H$_2$SO$_4$ (15 mL), K$_2$S$_2$O$_8$ (1.0 g) and P$_2$O$_5$ (1.0 g) were mixed and heated to 353 K to produce dark-blue pre-oxidized graphite. The pre-oxidized graphite powder was then produced by washing with ultra-pure water and filtering with 0.45 μm filters until the solution pH became neutral.

The above product (2.0 g) was put into concentrated H$_2$SO$_4$ (273 K, 50 mL) containing NaNO$_3$ (1.0 g) with agitation to prevent the temperature of the mixture from exceeding 293 K. The mixture was kept at 6 h at 273 K. Then, KMnO$_4$ (6.0 g) was added gradually and agitated for 12 h at 308 K.

The above reactions were finished by adding ultra-pure water (280 mL) and H$_2$O$_2$ solution (30%, v/v, 5 mL) within 30 min. Subsequently, a bright yellow mixture appeared. The mixture was then washed with HCl (10%, v/v). The resulting solution was centrifuged and washed until the solution pH became neutral. Finally, the product was desiccated by freeze-drying for further experiments.

2.2.2 Preparation of PPy–GO. Graphite oxide (0.2 g) was dispersed in ultra-pure water (200 mL) with ultra-sonication for 1 h. Py monomer (0.5 mL) was then added and agitated for 1 h at room temperature. Subsequently, PPy–GO solution was produced by adding FeCl$_3$·6H$_2$O (3 g) into the above solution and continuing agitation for 2 h. The as-prepared PPy–GO solution was washed with ultra-pure water to remove excess impurities.

2.2.3 Preparation of magnetic PPy–GO. FeSO$_4$·7H$_2$O (0.667 g) and FeCl$_3$·6H$_2$O (1.000 g) were dissolved into the PPy–GO solution (250 mL) prepared above and mechanically agitated in inert atmosphere at 353 K for 30 min to completely load ferric and ferrous salts onto the PPy–GO. Ammonia solution (15 mL, 30%, v/v) was dropped after 2 h of reaction at 353 K to form magnetic nanoparticles, which were subsequently cooled, filtered and washed to remove residual base. The resulting magnetic PPy–GO composite was dried and stocked.

2.3 Adsorption experiments

A reserve solution of mercury(II) (1.0 g L^{-1}) was obtained by dissolving HgCl$_2$ (0.6767 g) in a mixed solution (500 mL) containing HCl (0.01%, v/v) and HNO$_3$ (0.1%, v/v). The test was

operated under various conditions, including different mercury(II) contents (20–100 mg L^{-1}), a range of reaction times (t), pH values (2–10), adsorbent amounts (0.01–0.09 g L^{-1}) and temperatures (T, 300–320 K).

The equilibrium adsorption capacities (q_e, mg g^{-1}) were determined by eqn (1):

$$q_e = \frac{(C_0 - C_e)}{W} \times V, \tag{1}$$

where C_0 and C_e are the original and residual concentrations of mercury(II) (mg L^{-1}), respectively, V (L) is the solution volume, and W (g) is the adsorbent dosage. For convenience, adsorbent dosage was expressed as the ratio of solid to liquid (RSL, g L^{-1}).

2.3.1 Experiments of pH effect. The test was operated by adding magnetic PPy–GO adsorbent (0.005 g) into a conical flask (250 mL) containing a mercury(II) solution (100 mL, 20 mg L^{-1}). The flask was placed in a thermostatic shaker and agitated at 170 rpm at 300 K for 10 h to achieve equilibrium. The solution pH was changed between 2 and 10 by adding HCl or NaOH (0.1 M) with the aid of a pH instrument (PB-10, Sartorius, Germany).

2.3.2 Experiment of dosage effect. The dosage effect on the capacity to adsorb mercury(II) was determined using RSL values (0.01–0.09 g L^{-1}). The values of C_0, pH and solution volume were 20 mg L^{-1}, 7 and 100 mL, respectively. The removal efficiency E (%) of mercury(II) was calculated from the difference between C_0 and C_e.

2.3.3 Experiment of coexisting ions effect. The experiment was carried out for 10 h in NaNO$_3$ solution with Na$^+$ concentration in the range of 0.01–0.20 mol L^{-1} under the conditions of pH = 7.0 ± 0.1, RSL = 0.05 g L^{-1}, T = 300 K and C_0 = 20 mg L^{-1}.

2.3.4 Experiment of adsorption isotherms. The isotherm data were generated at RSL = 0.05 g L^{-1}, T = 300–320 K, pH = 7.0 ± 0.1 and various C_0 values (20–100 mg L^{-1}). The instantaneous capacities for mercury(II) (q_t, mg g^{-1}) were calculated by eqn (2):

$$q_t = \frac{(C_0 - C_t)}{W} \times V, \tag{2}$$

where C_t (mg g^{-1}) represents adsorbate content at time t (min).

2.3.5 Experiments of adsorption kinetics. The test was performed by adding magnetic PPy–GO adsorbent (0.015 g) into a conical flask (500 mL) containing mercury(II) solution (300 mL, 20 mg L^{-1}). The flask was placed in a thermostatic shaker and agitated at 170 rpm at 300 K. At various times t (20–720 min), 3 mL samples were withdrawn and then filtered to measure mercury(II) concentration.

2.4 Analytical methods

The BET value was determined from the nitrogen adsorption/desorption plot using a specific surface area analyzer (V-Sorb 2800TP, Gold APP, China). The textural properties and surface morphologies were characterized by SEM (ZEISS, Germany) and TEM (JEM-2100, Japan). The elemental analysis was obtained by EDX.

Analyses of the organic functional groups and lattice structure were conducted *via* FT-IR (Nicolet 6700, Thermo-Nicolet,

USA) and XRD (D8 Advance, Bruker, Germany). The range of diffraction angles (2θ) was 5° to 80°.

An electrophoresis analyzer (ZetaPALS, Brookhaven, USA) was employed to determine the zeta potential values of the absorbents under different pH values. An XPS meter (250Xi, Thermo-VG Scientific, USA) was applied to analyze the element valence state. The magnetic property was confirmed by a VSM meter (Lakeshore 7404, USA) with a 10 kOe magnetic field at 298 K. The contents of mercury(II) ions were analyzed by cold atomic absorption adsorption spectrophotometry (F732-VJ, Jiangfeng, China).

3. Results and discussion

3.1 Characterization

3.1.1 Surface morphology. The SEM images shown in Fig. 1(a) and (b) show that the magnetic PPy–GO had a cauliflower-like and granular morphology, implying the successful polymerization of Py monomer on the surface of GO.[25] The TEM image of magnetic PPy–GO [Fig. 1(c)] shows a folded lamellar structure. This structure is attributed to the unique attributes of GO, which may provide a large BET value and more adsorption sites. EDX elemental analysis [Fig. 1(d)] confirmed the presence of C, O, Fe and N elements. All of these results suggested that the Fe$_3$O$_4$ and PPy materials successfully combined with the GO nanocomposite to form the magnetic PPy–GO nanocomposite. The TEM and SEM images show that the Fe$_3$O$_4$ nanoparticles and PPy polymer were all loaded on the surface of GO, taking full advantage of the large specific surface area of GO.

The combination of PPy, GO and Fe$_3$O$_4$ nanoparticles is conducive to improving the drawbacks of PPy and GO mentioned above by increasing the density, size and BET values of the composite nanomaterials and improving their dispersion in water so as to enhance the adsorption capacity for heavy metals.

3.1.2 Textural characterization. The textural characteristics of the materials are displayed in Fig. 2. From Fig. 2(a), it can draw a conclusion that the isotherm of the magnetic PPy–GO exhibited an obvious H4 hysteresis loop, which shows that the magnetic PPy–GO was a typical mesoporous material with pore size between 2 and 50 nm [Fig. 2(b)]. All of the morphologies agreed with the SEM and TEM images. The BET value of GO was 515.8 m^2 g^{-1}. After combining GO with PPy, the BET value of the magnetic PPy–GO increased remarkably by 236.8% and reached 1737.6 m^2 g^{-1}. The increased BET value was conducive to the performance of magnetic PPy–GO for removing mercury(II).

The pore size distribution of magnetic PPy–GO is shown in Fig. 2(b). The average pore diameter and pore volume were 4.2 nm and 0.89 cm^3 g^{-1}, respectively. According to the BET determination, it can draw a conclusion that the characteristics of the magnetic PPy–GO will be conducive to adsorbing mercury(II).

3.1.3 XRD. The XRD image in Fig. 3 shows that GO typical diffraction peaks appeared at 11.2° and 42.6°.[26] In the diffraction pattern of the magnetic PPy–GO, five peaks were observed at 30.3°, 35.7°, 43.3°, 57.0° and 62.9°; these are the

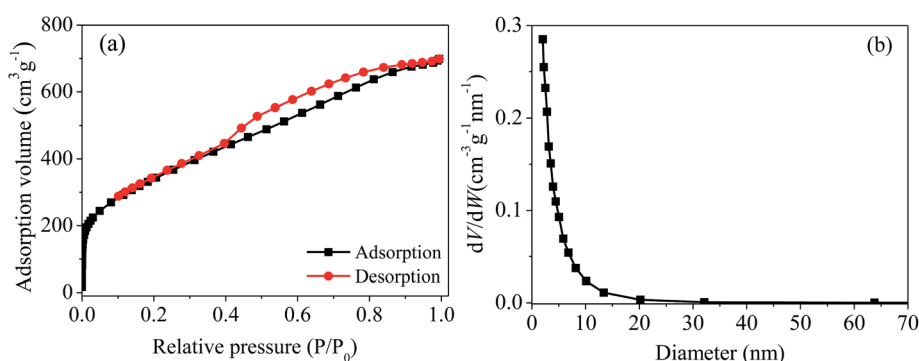**Fig. 1** SEM (a) and (b), TEM (c), and EDX (d) images of magnetic PPy–GO.

Fig. 2 N₂ adsorption/desorption plots (a) and pore size distribution (b).

characteristic diffraction peaks of iron oxides in magnetic PPy–GO[27] and belong to the crystal planes of Fe_3O_4 (JCPDS no. 085-1436).

Moreover, no peaks of Ppy were observed; these peaks may have been completely covered by the strong diffraction peaks of Fe_3O_4 due to the effects of the magnetic nanoparticles in the magnetic PPy–GO.[9]

3.1.4 Surface functional groups. FT-IR spectra (shown in Fig. 4) were employed to determine the functional groups of the prepared materials. The peaks at 3132.8 and 3418.9 cm^{-1} resulted from the vibration of hydroxyl.[17] The vibrations at 1713.5 and 1633.2 cm^{-1} are attributed to carbonyl and carboxyl groups (C=

O).[17] The strong peaks appearing at 1600.1 and 1540.3 cm^{-1} were related to the C=C bonds in the GO and Py rings, respectively, further confirming the presence of polypyrrole.[28]

The obvious peak at 1460.1 cm^{-1} could be attributed to the C–H stretching vibration in the structure of the pyrrole ring.[28] The peaks at near 1380 cm^{-1} correspond to the vibrations of C–O in the carboxyl groups.[29] The two peaks at around 1373 cm^{-1} correspond to C–N bond stretching vibrations in the structure of the pyrrole ring.[28,30] The presence of the peak at 1160.3 cm^{-1} indicated the presence of C–O–C bonds in the GO rings.[30] A very strong band at 1034.1 cm^{-1} was assigned to the
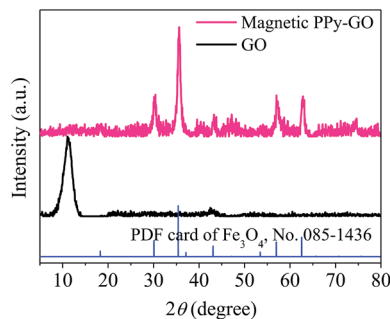
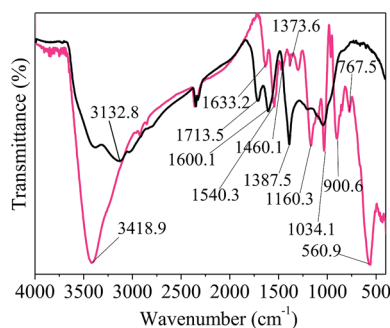**Fig. 3** XRD patterns of GO and magnetic PPy–GO.

Fig. 4 FT-IR spectra of GO (black curve) and magnetic PPy–GO (pink curve).

in-plane deformation of the C–H and N–H bonds of the pyrrole ring.[30,31]

The adsorption bands at 900.6 and 767.5 cm^{-1} were attributed to the deformation and out-of-plane vibration of C–H or wagging vibration of pyrrole, respectively.[25,28] The peak at 560.9 cm^{-1} indicated the presence of Fe–O vibration and the successful combination of Fe_3O_4 nanocomposite with GO, which is consistent with the XRD data.

3.1.5 XPS. Comparing the wide-scan XPS spectra of PPy–GO and GO [Fig. 5(a)] indicates that some new Fe 2p and N 1s peaks appeared in the spectrum of magnetic PPy–GO, verifying that Fe_3O_4 and polypyrrole were successfully combined with GO.

In Fig. 5(b), the peaks at 283.7, 284.7 and 284.5 eV were all assigned to the C–C or/and C=C bonds in the ring structures of the magnetic PPy–GO and GO.[32] However, there was an obvious difference among the above three C 1s peaks because of the presence of sp^2 hybridized carbon.

The peak at 286.6 eV belonged to epoxy and alkoxy.[19,33] The peaks at 286.2 and 286.3 eV should correspond to the carbon-linking hydroxyl groups (C–OH) in GO.[16,33] The peaks at 287.3 and 287.7 eV should be attributed to carbonyl groups (C=O) in the structure of GO.[33] The peak located at 288.5 eV was assigned to the COOH groups in GO.[32,33]

The binding energies of Fe 2p$_{1/2}$ and 2p$_{3/2}$ were 710.3 and 723.8 eV, respectively [Fig. 5(c)]. As shown in Fig. 5(d), the peak belonging to O 1s moved from 531.7 eV for GO to 529.3 eV for magnetic PPy–GO, which can be attributed to the characteristics of lattice oxygen in the Fe_3O_4 nanoparticles. Moreover, the
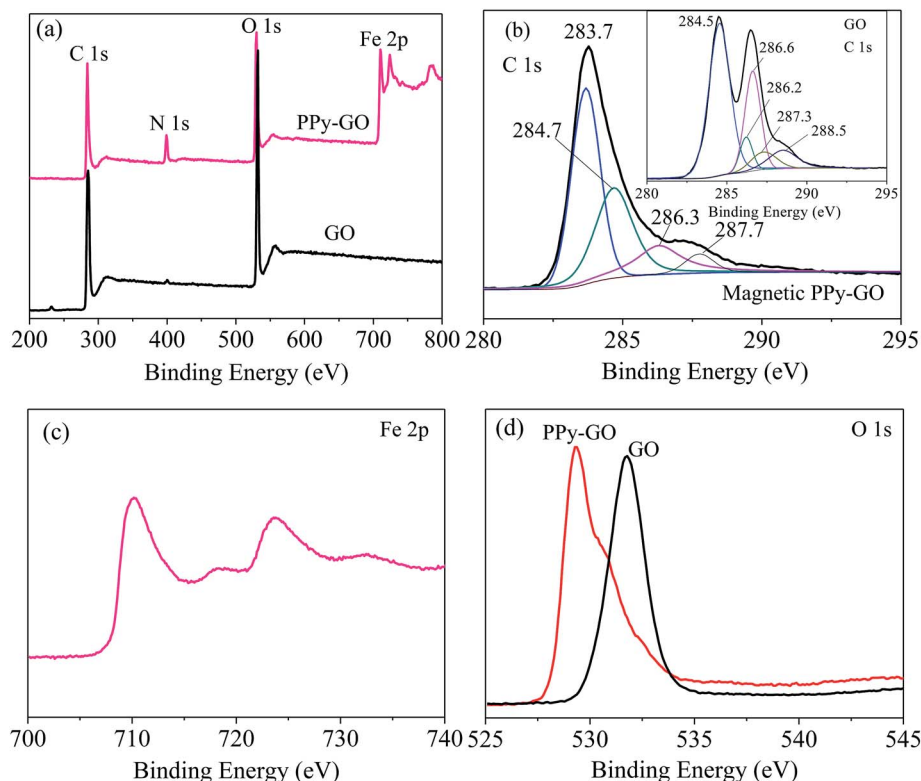

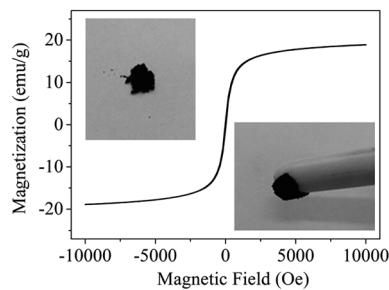**Fig. 5** XPS spectra: wide scan (a), C 1s (b), Fe 2p (c), and O 1s (d).

Fig. 6 Magnetization curve of the magnetic PPy–GO.
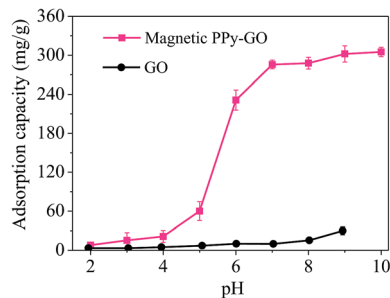

Fig. 8 Adsorption capacities of GO and magnetic PPy–GO under various pH conditions. Conditions: $T = 300$ K, RSL = 0.05 g L^{-1} and C_0 = 20 mg L^{-1} for magnetic PPy–GO; $T = 298$ K, RSL = 0.5 g L^{-1} and C_0 = 100 mg L^{-1} for GO.[32]

binding energy of N 1s at 399.3 eV (not shown) confirmed the presence and successful synthesis of PPy polymer.

3.1.6 Magnetization. Fig. 6 shows that the magnetization curve of the magnetic PPy–GO had an S-like hysteresis loop, and the value of saturation magnetization was 19.0 emu g^{-1}. Under the presence of an applied magnetic field, it was easy to separate the magnetic PPy–GO nanocomposite from an aqueous medium.

3.1.7 Electrochemical properties. The zeta potentials of the magnetic PPy–GO under different pH values are shown in Fig. 7 (pink curve). It can be observed that the magnetic PPy–GO nanocomposite possessed a positive charge at pH $\leq$ 6 and a negative charge at pH $\geq$ 6. The zeta potentials of magnetic PPy–GO quickly decreased with increasing pH, indicating that massive negative charges were generated on the surface of magnetic PPy–GO. This may be due to the dissociation or/and de-protonation of magnetic PPy–GO at high pH. This change was favorable for the removal of positively charged mercury(II). However, the zeta potentials of GO (black curve in Fig. 7) were all negative in a wide range from pH 3 to 10.

3.2 Adsorption studies

3.2.1 Effect of pH. The pH can significantly affect the surface charges of adsorbents, ionic states of oxygen-containing functional groups and ionic species of metals.[12,34,35] The influence of pH was evaluated at pH values of 2 to 10 (Fig. 8). As shown in Fig. 8, the adsorption performance of the magnetic PPy–GO strongly depended on solution pH, and the capacity for mercury(II) adsorption was enhanced with increasing pH. When pH was less than 5, the adsorption capacity was weak (below

60 mg g^{-1}). As the pH increased from 5 to 7, the adsorption capacity of the magnetic PPy–GO increased quickly and reached 285.7 mg g^{-1} at pH 7.0, much higher than the capacity of GO at pH 6.0 (10.0 mg g^{-1}).[32]

Upon further increasing the solution pH, the adsorption capacity of the magnetic PPy–GO continued to increase, but the rate of increase gradually became slow (pH greater than 7).

The existence morphologies of mercury(II) in water can explain the above phenomenon. The species of mercury present in water change with solution pH as follows: main Hg^{2+} and minor HgCl$^+$ (pH less than 4.0); main HgCl$_2$ and trace Hg(OH)$_2$ (pH 4–6); HgCl$_2$, HgOH$^+$, Hg(OH)$_3{}^+$ and minor Hg(OH)$_2$ (pH of 6–8); and mainly insoluble Hg(OH)$_2$ (pH greater than 8).[36-38]

At low pH, the electrostatic repulsion between magnetic PPy–GO and Hg^{2+} hindered the removal of mercury(II). With the increase in pH from 5 to 7, the surface of magnetic PPy–GO became negatively charged, which was beneficial to the adsorption of Hg^{2+} and Hg(OH)$_2$. The increase in negative charges on the surface of magnetic PPy–GO was obvious (see the zeta potential shown in Fig. 7), corresponding to the quick increase in adsorption capacity.

However, when solution pH was greater than 7, the increase in the adsorption capacity of the magnetic PPy–GO gradually became slow, which should be attributed to the deposition of mercury ions as Hg(OH)$_2$ ($K_{sp} = 3.13 \times 10^{-26}$), resulting in the removal of mercury(II).[39] Simultaneously, this might have originated from the lone electron pairs of the nitrogen atoms that coordinated with Hg^{2+} to form relatively stable complexes, promoting the further removal of mercury(II).[30] Additionally, some active sites with negative charges would be produced from the de-protonation of oxygen-containing functional groups and PPy polymer at higher pH.[39] Thus, a pH of 7 was selected as the subsequent experimental value.

3.2.2 Effect of dosage. The influence of adsorbent dosage on mercury(II) removal is shown in Fig. 9. Based on the data, increasing the absorbent dosage promoted the removal efficiency of mercury(II). The efficiency was increased from 16.0% (RSL = 0.01 g L^{-1}) to 98.1% (RSL = 0.09 g L^{-1}), corresponding to a q_e of 319.0 and 218.0 mg g^{-1}, respectively. With increasing RSL, the active sites of the adsorbents also increased, promoting binding between the magnetic PPy–GO and mercury(II).[40]

Fig. 7 Zeta potentials of GO and magnetic PPy–GO.

Fig. 9 Effects of adsorbent dosage on the removal of mercury(II). Condition: $T = 300$ K, $C_0 = 20$ mg L^{-1}, pH = 7.0 ± 0.1.

3.2.3 Effect of coexisting ions.

Coexisting metal ions affect many aspects of the adsorption process. For example, coexisting ions can compete for the limited active sites, influence electrostatic interactions and impede the transfer of metal ions from solution to the adsorbent surface.[13] To understand the impact of coexisting metal ions, experiments were carried out with different concentrations of sodium ions to examine the adsorption capacity of the magnetic PPy–GO. The results are displayed in Fig. 10. As the concentration of sodium ions increased, the adsorption capacity for mercury(II) decreased slightly, indicating that sodium ions had a weak effect on mercury(II) adsorption onto the magnetic PPy–GO.

Some literature pointed out that alkali metal ions including Na$^+$ and K$^+$ can compete with mercury(II) for the limited active sites due to the electrostatic effect.[41] The experimental results showed that increasing the ionic concentration could increase competitive adsorption between Na$^+$ cations and mercury(II). It is clear that electrostatic effects play a significant role during the adsorption of mercury(II).

3.2.4 Effect of reaction time.

The experimental results regarding the effect of reaction time are displayed in Fig. 11. Based on Fig. 11, the adsorption capacity of the magnetic PPy–GO increased rapidly but evenly over a long time period (0–120 min) with increasing contact time. Subsequently, the rate of increasing adsorption gradually decreased and reached an equilibrium state after approximately 600 min. Correspondingly, the maximum $q_{e,exp}$ of the magnetic PPy–GO was 285.7 mg g^{-1} in the equilibrium state. However, the adsorption capacity of GO only increased slightly with time, and the maximum $q_{e,exp}$ of GO was only 13.0 mg g^{-1}.[32]

Fig. 10 Effect of ionic strength on the removal of mercury(II). Condition: $T = 300$ K, $C_0 = 20$ mg L^{-1}, RSL = 0.05 g L^{-1}, pH = 7.0 ± 0.1.

Fig. 11 Effect of time on the removal of Hg(II) with GO and magnetic PPy–GO. Conditions: $T = 300$ K, $C_0 = 20$ mg L^{-1}, RSL = 0.05 g L^{-1} and pH = 7.0 ± 0.1 for magnetic PPy–GO; $T = 298$ K, RSL = 0.5 g L^{-1}, $C_0 = 100$ mg L^{-1} and pH = 6.0 for GO.[32]

The above results are attributed to the many active metal-binding sites on the surface of the magnetic PPy–GO at the beginning of the experiment. After a period of time, it became difficult for mercury(II) to occupy the remaining active sites because fewer adsorption sites were available, and the repulsive forces between the mercury(II) on the surface of the magnetic PPy–GO and mercury(II) in the solution phase. Additionally, the concentration gradients of mercury(II) between the solid surface and liquid-phase surface gradually decreased, resulting in a decelerating adsorption rate.

3.3 Adsorption kinetics

Adsorption kinetics can not only give a clear relationship between the adsorption amount of mercury(II) and contact time, but also provide some necessary information about the adsorption mechanism.[42] To study the kinetic process of the adsorption for mercury(II), pseudo-first-order [eqn (3)] and pseudo-second-order kinetic models [eqn (4)] were used to investigate and fit the experimental results:

$$\ln(q_e - q_t) = \ln q_e - k_1 t \qquad (3)$$

and

$$\frac{t}{q_t} = \frac{1}{q_e^2 k_2} + \frac{t}{q_e}, \qquad (4)$$

where k_1 (min^{-1}) and k_2 (mg mg^{-1} min^{-1}) are rate constants.

Normally, the intra-particle model [eqn (5)] is employed to study the diffusion occurring in the inter-crystalline spaces of the adsorbent, particularly for GO-based materials:

$$q_t = k_{di} t^{0.5} + C_i \qquad (5)$$

where k_{di} (mg g^{-1} min$^{-0.5}$) and C_i (mg g^{-1}) are the diffusion coefficient and boundary-layer thickness at stage i, respectively. In comparison, the Elovich equation is hardly influenced by subjective factors and can be determined via eqn (6):

$$q_t = \frac{1}{\beta} \ln(\alpha\beta) + \frac{1}{\beta} \ln t, \qquad (6)$$

where α (mmol g^{-1} min^{-1}) and β (g mmol^{-1}) are the adsorption and desorption constants, respectively.

Table 1 Parameters of the kinetic models

Pseudo-first-order				Pseudo-second-order		
$q_{e,exp}$ (mg g^{-1})	$q_{e,cal}$ (mg g^{-1})	k_1 (min^{-1})	R_1^2	$q_{e,cal}$ (mg g^{-1})	k_2 (mg mg^{-1} min^{-1})	R_2^2
285.7	349.7	0.0062	0.974	321.7	0.189	0.998

Intra-particle diffusion								
k_{d1} (mg g^{-1} min$^{-0.5}$)	C_1 (mg g^{-1})	R_1^2	k_{d2} (mg g^{-1} min$^{-0.5}$)	C_2 (mg g^{-1})	R_2^2	k_{d3} (mg g^{-1} min$^{-0.5}$)	C_3 (mg g^{-1})	R_3^2
15.17	−18.93	0.996	8.76	76.16	0.994	2.68	215.11	0.999

Elovich model					
α_1 (mmol g^{-1} min^{-1})	β_1 (g mmol^{-1})	R_1^2	α_2 (mmol g^{-1} min^{-1})	β_2 (g mmol^{-1})	R_2^2
1026.49	0.013	0.987	148.25	0.028	0.999

The above four models can produce different lines, indicating a composite adsorption process that includes film diffusion, exterior surface diffusion and intra-particle diffusion.[43] Based on the literature, the plot of $t^{0.5}$ vs. q_t will be linear if the process of intra-particle mass-transfer is involved.[43]

According to the fitted kinetic results shown in Table 1, the linear regression coefficient R_2^2 (0.998) of the pseudo-second-order kinetic model was higher than the coefficient ($R_1^2 = 0.974$) of the pseudo-first-order kinetic model [Fig. 12(a) and (b)]. The $q_{e,cal}$ value of the pseudo-second-order equation was more relevant to the experimental value $q_{e,exp}$. Hence, the removal process of mercury(II) ions

conformed to pseudo-second-order model and involved some chemisorption.

The plots in Fig. 12(c) show three linear stages, indicating an adsorption process controlled by three stages. The values of K_{di}, C_i and R^2 in three stages are tabularized in Table 1.

The initial stage from $4.47^{0.5}$ to $15.49^{0.5}$ exhibited a sharp gradient attributed to exterior surface diffusion or film diffusion, corresponding to an instantaneous adsorption process ($K_{d1} = 15.17$) and indicating that a large amount of mercury(II) was quickly adsorbed via the external plane of the adsorbent. The second stage from $15.49^{0.5}$ to $24.49^{0.5}$ was attributed to intra-particle diffusion. The third stage (plateau stage) from
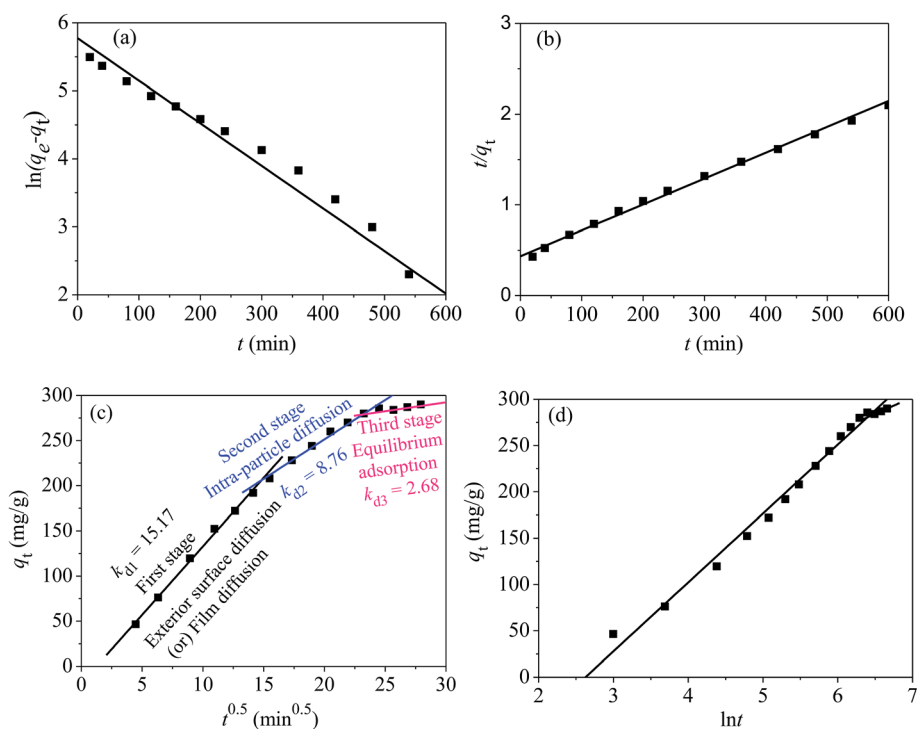

Fig. 12 Pseudo-first-order kinetic model (a), pseudo-second-order kinetic model (b), intra-particle diffusion kinetics (c) and Elovich model (d) for the adsorption of mercury(II) onto the magnetic PPy–GO.

$24.49^{0.5}$ to $27.93^{0.5}$ belonged to equilibrium adsorption and represented a gradual saturation adsorption process.

The values of K_{di} that represent the diffusion rates at different points during the adsorption process are tabulated in Table 1. Adsorption rate decreased in the following order: $K_{d1} > K_{d2} > K_{d3}$. This is explained as follows. As adsorption on the external surface reached saturation, the rate of mercury(II) penetrating into the inter-crystalline regions of magnetic PPy–GO was gradually decreased and finally reached an equilibrium stage ($K_{d3} = 2.68$).

Moreover, C_i (shown in Table 1) was not equal to zero, indicating that the adsorption of mercury(II) involved some chemisorption and was partially controlled by intra-particle diffusion.[18,44]

Fig. 12(d) shows a linearized plot based on the Elovich model. The intercept and slope of the plot are normally employed to determine the initial adsorption rate α and constant β. From Fig. 12(d) it can be seen that α_i was greater than β_i at each fitting segment. In addition, the desorption coefficient β_2 (0.028) was higher than β_1 (0.013), indicating a gradually decelerating adsorption process trending towards an equilibrium stage; these findings were consistent with the fitting results from intra-particle diffusion.

The above results reveal that the general adsorption process of mercury(II) onto magnetic PPy–GO was controlled by chemical adsorption.
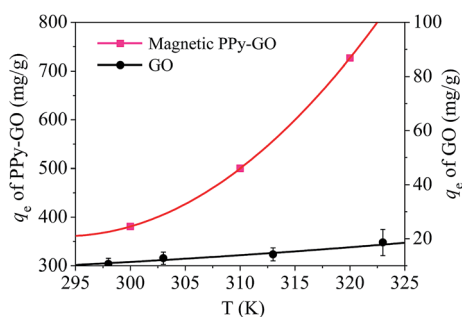
3.4 Adsorption isotherms

Adsorption isotherms are key to optimizing the application of adsorbents as they can be used to assess the performance of the adsorbent as well as to describe the interactions between adsorbates and adsorbents.[9] For the sake of assessing the effect of temperature on the adsorption process, adsorption isotherms were constructed at various temperatures from 300 to 320 K.

The temperature effect (Fig. 13) reveals that the adsorption capacity of magnetic PPy–GO was enhanced as temperature increased, indicating a preferable adsorption performance at higher temperatures. In comparison, the adsorption capacity of GO was only slightly enhanced as the temperature increased from 298 to 323 K. This results is explained as follows. As the temperature increased, the interaction between the solvent and adsorbent surface decreased, leading to more available adsorption sites.

The Langmuir and Freundlich equations are often employed for analyzing thermodynamic parameters. The Langmuir model considers homogeneous, monolayer adsorption with no inter-reaction between the adsorbed molecules and is given in linear form by eqn (7):

$$\frac{C_e}{q_e} = \frac{C_e}{Q_m} + \frac{1}{Q_m K_L}, \tag{7}$$

where Q_m (mg g^{-1}) represents the maximum adsorption capacity, and K_L (L mg^{-1}) is a constant connected to enthalpy. The Freundlich model given by eqn (8) is normally employed to explain multilayer heterogeneous adsorption:

$$\ln q_e = \ln K_C + \frac{1}{n} \ln C_e, \tag{8}$$

where $1/n$ is an empirical value that is connected with adsorption intensity and varies with the heterogeneity of the adsorption material, and K_C is a constant connected with adsorption capacity. The separation factor (R_L) used to describe adsorption characteristics can be calculated with K_C using eqn (9):[45]

$$R_L = \frac{1}{1 + K_L C_0}. \tag{9}$$

Fig. 13 Adsorption isotherms of mercury(II) onto the magnetic PPy–GO nanocomposite. Conditions: pH = 7 ± 0.1, RSL = 0.05 g L^{-1} and C_0 = 100 mg L^{-1} for the magnetic PPy–GO; pH = 6, RSL = 0.5 g L^{-1} and C_0 = 100 mg L^{-1} for the GO.[32]

The parameters of the adsorption isotherms (Fig. 14) for the adsorption of mercury(II) onto the magnetic PPy–GO at various temperatures are listed in Table 2.
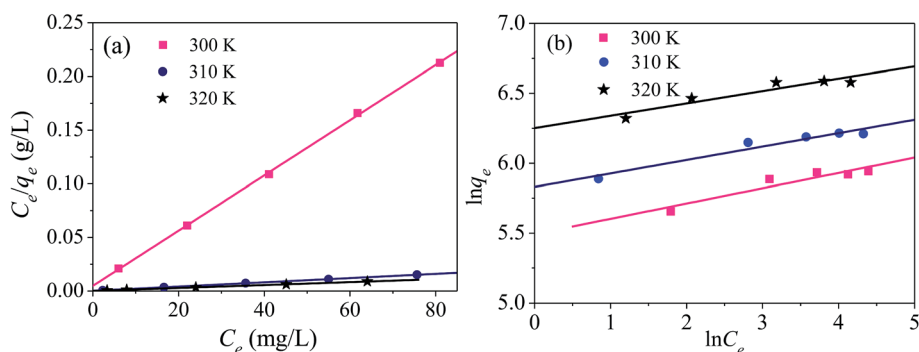

Fig. 14 Adsorption isotherms for the adsorption of mercury(II) onto magnetic PPy–GO: Langmuir (a) and Freundlich (b) models. Conditions: pH = 7 ± 0.1, RSL = 0.05 g L^{-1}, C_0 = 20–100 mg L^{-1}.

Table 2 Parameters of the isotherm models

Experimental conditions	Langmuir				Freundlich		
	Q_m (mg g^{-1})	K_L (L mg^{-1})	R_1^2	R_L	$1/n$	K_C (mg^{1-n} L^n g^{-1})	R_2^2
$T = 300$ K	400.0	0.52	0.999	0.019	0.109	243.0	0.841
$T = 310$ K	526.3	0.86	0.999	0.011	0.096	340.7	0.924
$T = 320$ K	769.2	1.08	0.999	0.009	0.088	518.7	0.852

In comparison with Freundlich model, the Langmuir model was more consistent with the adsorption of mercury(II) based on correlation coefficient R^2, indicating monolayer adsorption. The maximum adsorption capacities of mercury(II) were 400.0 mg g^{-1} ($T = 300$ K) and 769.2 mg g^{-1} ($T = 320$ K).

According to the data obtained from Fig. 14, the values of R_L were determined to be 0.019 ($T = 300$ K), 0.011 ($T = 310$ K) and 0.009 ($T = 320$ K). Normally, the separation factor R_L represents favorable adsorption ($0 < R_L < 1$), linear adsorption ($R_L = 1$), irreversible adsorption ($R_L = 0$) or unfavorable adsorption ($R_L > 1$).[1,46] The obtained values of R_L were less than one, indicating favorable adsorption of mercury(II) onto the magnetic PPy–GO.

Smaller values of $1/n$ indicate a higher adsorption intensity and the involvement of a chemical process during the adsorption of mercury(II), in agreement with the larger K_C values obtained using the Langmuir model.

Based on the data of k_1, k_2, K_L and K_C from kinetics and isotherm models, respectively, it can be concluded that it is easy for mercury(II) to adsorb onto the magnetic PPy–GO, and that the magnetic PPy–GO material has a higher adsorption rate and capacity. According to the above results and the adsorption data shown in Table 3, the adsorption capability of magnetic PPy–GO for mercury(II) surpasses the performances of many other adsorbents, indicating that the magnetic PPy–GO material is a promising adsorbent.

3.5 Adsorption thermodynamics

The thermodynamic performance of the magnetic PPy–GO material for mercury(II) adsorption was examined and evaluated *via* Gibbs free energy (ΔG^0), standard entropy [ΔS^0 (J mol^{-1} K^{-1})] and standard enthalpy [ΔH^0 (kJ mol^{-1})] using eqn (10):

$$\ln K_d = \frac{\Delta S^0}{R} - \frac{\Delta H^0}{RT}, \qquad (10)$$

where R is the universal gas constant, K_d is a thermodynamic equilibrium constant without units. ΔS^0 can be determined from the Langmuir equilibrium constant K_L.[61]

The value of ΔG^0 can be determined by eqn (11):

$$\Delta G^0 = -RT \ln K_d, \qquad (11)$$

where ΔG^0 is the standard free energy (kJ mol^{-1}).

The values of ΔG^0, ΔS^0 and ΔH^0 are shown in Fig. 15, and the corresponding data are listed in Table 4. Fig. 15 shows that the adsorption for mercury(II) had an endothermic nature and involved certain chemical reactions because of the large positive ΔH^0.[46] The adsorption of mercury(II) was influenced by temperature and had randomness on the solid–liquid surface based on positive ΔS^0.[61]

The negative ΔG^0 suggested a feasible and spontaneous adsorption process.[46,61] In addition, the decreasing ΔG^0 with increasing temperature revealed that mercury(II) adsorption

Table 3 Comparison of adsorption capacities of various absorbents for mercury(II)

| Adsorbents	BET (m^2 g^{-1})	Q_m (mg g^{-1})	Ref.
Magnetic PPy–GO	1737.6	400.0 (pH = 7)	This work
GO	9.2	32.7 (pH = 6)	32
Magnetic GO (MGO)	58.6	71.3 (pH = 6)	32
3D reduced graphene oxide aerogel		185 (pH = 6)	47
Glutamine-modified chitosan magnetic composite microspheres		199.2 (pH = 5)	48
Poly-dithiocrabamate series	Less than 12	22.1 (pH = 5)	49
Coal-based activated carbon	900	48.9 (pH = 4)	50
Chitosan-coated magnetic nanoparticles		10 (pH = 3)	51
MnO$_2$/CNT nanocomposites	110.4	58.8 (pH = 6)	52
Multi-walled carbon nanotubes		13.2 (pH = 8)	53
Multi-walled carbon nanotubes	270	25.6 (pH = 7)	54
Dithizone-immobilized zeolite		2.6 (pH = 7)	39
Bamboo leaf powder		27.1 (pH = 8)	55
Synthetic terpolymer		53.5 (pH = 4.5)	56
Chitosan		56 (pH = 5)	57
Magnetic porous microspheres	86.4	28.3 (pH = 7.4)	58
Biochar	4.5	8 (pH = 7.7)	59
Natural pyrite	20.1	80.2 (pH = 8)	60
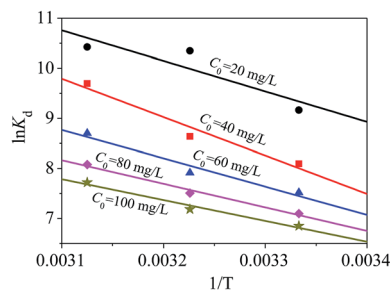
Fig. 15 Thermodynamic fits for mercury(II) removal onto magnetic PPy–GO.

Fig. 16 XRD patterns of the magnetic PPy–GO after use.

Table 4 Thermodynamic parameters of mercury(II) adsorption onto magnetic PPy–GO

C_0 (mg L^{-1})	ΔH^0 (kJ mol^{-1})	ΔS^0 (J mol^{-1} K^{-1})	ΔG^0 (kJ mol^{-1})		
			300 K	310 K	320 K
20.0	50.7	246.6	−22.9	−26.7	−27.7
40.0	63.8	279.1	−20.2	−22.3	−25.8
60.0	47.1	218.9	−18.8	−20.4	−23.2
80.0	39.2	189.5	−17.7	−19.4	−21.5
100.0	34.7	172.4	−17.1	−18.5	−20.5

onto magnetic PPy–GO was more advantageous at higher temperature, which was consistent with the data shown in Fig. 13. The small ΔG^0 (less than −40 kJ mol^{-1}) indicated that the interaction between adsorbed mercury(II) and the magnetic PPy–GO material involved a strong chemical reaction.[46]

3.6 Stability of magnetic PPy–GO

To evaluate the stability of the adsorbent, magnetic PPy–GO was separated after reaction, rinsed three times with 0.5 L ethanol solution (10 vol% HCl acid) and 1 L ultra-pure water, and then dried at 378 K. Adsorbent stability was evaluated at two different reaction conditions (pH = 4.0 and pH = 7.0) based on the regeneration performance. Based on the test data (not shown), the decreases in the adsorption capacities of the magnetic PPy–GO at pH 4.0 and 7.0 were about 15.8% and 13.7% after three cycles and 20.8% and 22.7% after five cycles, respectively.

The results indicated that the pH of the solution containing mercury(II) affected the adsorption capacity of the as-prepared adsorbent. This result might be related to the speciation mercury(II) and the charge of the adsorbent at different pH values. The isoelectric point of Fe$_3$O$_4$ is pH = 6.5; thus, Fe$_3$O$_4$ possesses a positive charge at pH ≤ 6.5 and a negative charge at pH ≥ 6.5, similar to the magnetic PPy–GO.

To further investigate the stability of the as-prepared adsorbent, XRD was employed to characterize the magnetic PPy–GO after reaction at pH 4.0 and 7.0. Based on the XRD patterns shown in Fig. 16, there is little difference in peak position before and after use at pH 4.0 and 7.0. These results suggest that the as-prepared magnetic PPy–GO is relatively stable.

3.7 Removal of mercury(II) from real electroplating effluent

Electroplating wastewater is a serious pollutant of the environment and water bodies and contains many types of poisonous and harmful substances, including massive heavy metals in addition to organics. Some heavy metal ions in electroplating wastewater, particularly mercury, chromium, nickel and lead, cause serious harm to the human body and organisms. Conventional methods including chemical precipitation and biological treatment cannot completely remove all these heavy metal ions to meet the Chinese national standard of "Emission Standard of Pollutants for Electroplating" (GB 21900-2008). Therefore, adsorption may represent a more suitable method for the treatment of electroplating wastewater.

To investigate the potential for applying the as-prepared magnetic PPy–GO adsorbent in real wastewater treatment, real electroplating wastewater (after pre-treatment) was used as a raw wastewater sample to be treated. The wastewater was obtained from the effluent of a local company, Suzhou Third Electroplating Co., Ltd. The concentrations of mercury(II), chromium(VI), nickel(II), lead(II) and iron(III) were 0.05–0.1, 0.8–1.5, 0.8–2.2, 0.3–0.6 and 2.5–5.0 mg L^{-1}, respectively. The COD$_{cr}$ value of the wastewater was about 50–70 mg L^{-1}. The experiment was carried out three times to obtain an average efficiency under the conditions of RSL = 0.05 g L^{-1} and pH = 7 ± 0.2.

The results show that the removal efficiency of total mercury reached over 99%, and the removal efficiencies of other the metal ions were over 80%. The effluent quality after adsorption basically met the Chinese national standard with the exception of a slight excess of chromium(VI). The results show that the as-prepared magnetic PPy–GO material is indeed a potential adsorbent and can be used as a base material to adsorb heavy metals.
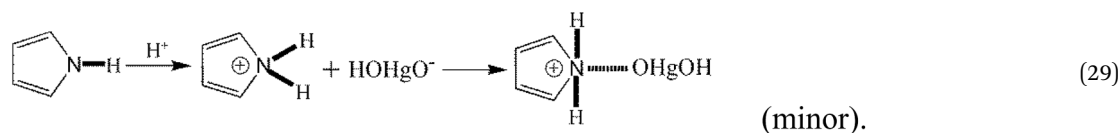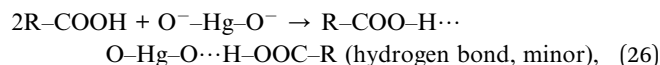
3.8 Adsorption mechanism

The experimental results indicated that pH had an obvious effect on the removal of mercury(II). In addition, the zeta potentials and FT-IR data showed that oxygen-containing functional groups played a significant role in the removal of mercury(II). The zeta potentials also indicated that the quantity of negative charges possessed by magnetic PPy–GO increased significantly with increasing solution pH, which was beneficial to the adsorption of positively charged mercury(II) via electrostatic attraction.

The results of adsorption experiments and Langmuir fitting showed that the magnetic PPy–GO had a high adsorption capacity for mercury(II). The main possible mechanism included the formation of ionic pairs, hydrogen bonding between oxygen-containing functional groups and various mercury species (Hg^{2+}, $HgOH^+$, $Hg(OH)_3^+$, $HgCl^+$, $HOHgO^-$ and $^-OHgO^-$), ion exchange, and electrostatic attraction. Moreover, these above morphologies of mercury had a more favorable size and higher mobility than Hg^{2+}, resulting in a higher adsorption capability for mercury(II).

The possible interactions between the magnetic PPy–GO and various mercury(II) species are formulated as follows:

$$R–OH \rightarrow R–O^- + H^+$$
(dissociation and de-protonation, major), (12)

$$R–COOH \rightarrow R–COO^- + H^+$$
(dissociation and de-protonation, major), (13)

$$2R–O^- + Hg^{2+} \rightarrow R–O–Hg–O–R$$
(ionic-pair formation, more major), (14)

$$2R–COO^- + Hg^{2+} \rightarrow R–COO–Hg–OOC–R$$
(ionic-pair formation, more major), (15)

$$R–O^- + R–COO^- + Hg^{2+} \rightarrow R–O–Hg–OOC–R$$
(ionic-pair formation, more major), (16)

$$R–O^- + HgOH^+ \rightarrow R–O\cdots HgOH$$
(electrostatic attraction, major), (17)

$$R–COO^- + HgOH^+ \rightarrow R–COO\cdots HgOH$$
(electrostatic attraction, major), (18)

$$R–O^- + Hg(OH)_3^+ \rightarrow R–O\cdots Hg(OH)_3$$
(electrostatic attraction, major), (19)

$$R–COO^- + Hg(OH)_3^+ \rightarrow R–COO\cdots Hg(OH)_3$$
(electrostatic attraction, major), (20)

$$R–COO^- + HgCl^+ \rightarrow R–COO\cdots HgCl$$
(electrostatic attraction, major), (21)

$$R–O^- + HgCl^+ \rightarrow R–O\cdots HgCl$$
(electrostatic attraction, major), (22)

$$R–O–H + H–O–Hg–O^- \rightarrow R–O–H\cdots O–Hg–OH$$
(hydrogen bond, minor), (23)

$$2R–O–H + O^-Hg–O^- \rightarrow$$
$$R–O–H\cdots O–Hg–O\cdots H–O–R \text{ (hydrogen bond, minor),} \quad (24)$$

$$R–COOH + HO–Hg–O^- \rightarrow R–COO–H\cdots O–Hg–OH$$
(hydrogen bond, minor) and (25)

$$2R–COOH + O^-–Hg–O^- \rightarrow R–COO–H\cdots$$
$$O–Hg–O\cdots H–OOC–R \text{ (hydrogen bond, minor),} \quad (26)$$

(Dissociation and de-protonation, major), (27)

(major) and (28)

(minor). (29)

where R represents the magnetic PPy–GO.

In addition to the above equations, the PPy polymer can also react with various mercury species *via* electrostatic attraction after dissociation or/and de-protonation as follows:

The above reactions suggest that a large number of OH^- radicals can react with H^+ resulting from –OH, –COOH or Py polymer under high solution pH, promoting the reaction. Moreover, high solution pH is favorable for the adsorption of cationic mercury(II) with positive charge.

The fitting of kinetics and thermodynamics suggested that mercury(II) removal was favorable, occurred in three stages (an initial stage of exterior surface diffusion or film diffusion, intra-particle diffusion and a plateau stage of equilibrium adsorption), and involved some chemisorption.

In addition, thermodynamic study also showed that the adsorption processes for mercury(II) was endothermic and spontaneous, and there were strong chemical interactions between the adsorbed mercury(II) and the magnetic PPy–GO material.

4. Conclusions

In this work, a Fe_3O_4 magnetic nanomaterial (PPy–GO) was synthetized and characterized for the removal of mercury(II) ions. XRD, EDX, XPS and the measurement of magnetization properties demonstrated that the Fe_3O_4 and PPy nanoparticles were successfully combined with GO.

Solution pH had a strong influence on the adsorption of mercury(II). When solution pH and RSL were 7 and 0.05 g L^{-1}, respectively, the Langmuir adsorption capacity of the magnetic PPy–GO reached 400.0 mg g^{-1}. The content of Na^+ had a weak influence on mercury(II) adsorption. The pseudo-second-order and Langmuir models provided the best fits to the data. The overall adsorption process of mercury(II) onto magnetic PPy–GO involved chemisorption as well as intra-particle diffusion. The thermodynamics indicated that the adsorption of mercury(II) was endothermic and spontaneous.

The application of PPy–GO to the adsorption of heavy metals from real electroplating wastewater indicated that the magnetic PPy–GO material has a high adsorption efficiency. After the adsorption of mercury(II), the magnetic PPy–GO material could be easily separated from aqueous media. These results indicated that the magnetic PPy–GO material is a promising adsorbent for the removal of mercury(II) from aqueous media.

Acknowledgements

References

1 L. Tran, P. X. Wu, Y. J. Zhu, L. Yang and N. W. Zhu, *J. Colloid Interface Sci.*, 2015, **445**, 348.

2 A. A. Ismaiel, M. K. Aroua and R. Yusoff, *Chem. Eng. J.*, 2013, **225**, 306.

3 S. Siva, S. Sudharsan and R. S. Kannan, *RSC Adv.*, 2015, **5**, 79665.

4 M. F. Yardim, T. Budinova, E. Ekinci, N. Petrov, M. Razvigorova and V. Minkova, *Chemosphere*, 2003, **52**, 835.

5 O. Hakami, Y. Zhang and C. J. Banks, *Water Res.*, 2012, **46**, 3913.

6 A. Saria and M. Tuzen, *J. Hazard. Mater.*, 2009, **171**, 500.

7 D. K. Mondal, B. K. Nandi and M. K. Purkait, *J. Environ. Chem. Eng.*, 2013, **1**, 891.

8 B. Qiu, H. Gu, X. Yan, J. Guo, Y. Wang, D. Sun, Q. Wang, M. Khan, X. Zhang and B. Weeks, *J. Mater. Chem. A*, 2014, **2**, 17454.

9 X. Peng, W. Zhang, L. Gai, H. Jiang, Y. Wang and L. Zhao, *Chem. Eng. J.*, 2015, **280**, 197.

10 H. Wang, X. Yuan, G. Zeng, Y. Wu, Y. Liu, Q. Jiang and S. Gu, *Adv. Colloid Interface Sci.*, 2015, **221**, 41.

11 Z. Wu, X. Yuan, J. Zhang, H. Wang, L. Jiang and G. Zeng, *ChemCatChem*, 2017, **9**, 41.

12 S. Yang, L. Li, Z. Pei, C. Li, J. Lv, J. Xie, B. Wen and S. Zhang, *Colloids Surf., A*, 2014, **457**, 100.

13 P. Tan, J. Sun, Y. Y. Hu, Z. Fang, Q. Bi, Y. C. Chen and J. H. Cheng, *J. Hazard. Mater.*, 2015, **297**, 251.

14 Q. Yan, Z. Zhang, Y. Zhang, A. Umar, Z. Guo, D. O'Hare and Q. Wang, *Eur. J. Inorg. Chem.*, 2015, **2015**, 4182.

15 Y. Qin, M. Long, B. Tan and B. Zhou, *Micro Nano Lett.*, 2014, **6**, 125.

16 F. Gao, H. Gu, H. Wang, X. Wang, B. Xiang and Z. Guo, *RSC Adv.*, 2015, **5**, 60208.

17 Y. H. Wang, L. L. Li, C. N. Luo, X. J. Wang and H. M. Duan, *Int. J. Biol. Macromol.*, 2016, **86**, 505.

18 L. M. Cui, X. Y. Guo, Q. Wei, Y. G. Wang, L. Gao, L. G. Yan, T. Yan and B. Du, *J. Colloid Interface Sci.*, 2015, **439**, 112.

19 Z. Wu, H. Zhong, X. Yuan, H. Wang, L. Wang, X. Chen, G. Zeng and Y. Wu, *Water Res.*, 2014, **67**, 330.

20 H. Mahmud, A. K. O. Huq and R. B. Yahya, *RSC Adv.*, 2016, **6**, 14778.

21 M. Shafiabadi, A. Dashti and H. A. Tayebi, *Synth. Met.*, 2016, **212**, 154.

22 A. E. Chávez-Guajardo, J. C. Medina-Llamas, L. Maqueira, C. A. S. Andrade, K. G. B. Alves and C. P. de Melo, *Chem. Eng. J.*, 2015, **281**, 826.

23 N. I. Kovtyukhova, P. J. Ollivier, B. R. Martin, T. E. Mallouk, S. A. Chizhik, E. V. B. And and A. D. Gorchinskiy, *Chem. Mater.*, 1999, **11**, 771.

24 W. S. Hummers and R. E. Offeman, *J. Am. Chem. Soc.*, 1958, **80**, 1339.

25 N. H. Mthombeni, S. Mbakop, A. Ochieng and M. S. Onyango, *J. Taiwan Inst. Chem. Eng.*, 2016, **66**, 172.

26 H. Feng, B. Wang, T. Lin, N. Chen, N. Wang and B. Chen, *J. Power Sources*, 2014, **246**, 621.

27 M. Bhaumik, A. Maity, V. V. Srinivasu and M. S. Onyango, *J. Hazard. Mater.*, 2011, **190**, 381.

28 R. Karthik and S. Meenakshi, *Synth. Met.*, 2014, **198**, 181.

29 V. Gari and M. Kim, *Monatsh. Chem.*, 2015, **146**, 1445.

30 V. Chandra and K. S. Kim, *Chem. Commun.*, 2011, **47**, 3942.

31 Y. Wang, Y. Wang, X. Yan, S. Wu, L. Shao, Y. Liu and Z. Guo, *Chemosphere*, 2016, **153**, 485.

32 Y. F. Guo, J. Deng, J. Y. Zhu, X. J. Zhou and R. B. Bai, *RSC Adv.*, 2016, **6**, 82523.

33 J. W. Zhang, M. S. Azam, C. Shi, J. Huang, B. Bin, Q. X. Liu and H. B. Zeng, *RSC Adv.*, 2015, **5**, 32272.

34 W. Hou, X. Yuan, W. Yan, X. Chen, L. Leng, W. Hui, L. Hui and G. Zeng, *Chem. Eng. J.*, 2015, **262**, 597.

35 M. Zabihi, A. Ahmadpour and A. H. Asl, *J. Hazard. Mater.*, 2009, **167**, 230.

36 Z. Wang, J. Xu, Y. Hu, H. Zhao, J. Zhou, Y. Liu, Z. Lou and X. Xu, *J. Taiwan Inst. Chem. Eng.*, 2016, **60**, 394.

37 V. Chandra and K. S. Kim, *Chem. Commun.*, 2011, **47**, 3942.

38 J. Zhu, B. Deng, J. Yang and D. Gang, *Carbon*, 2009, **47**, 2014.

39 M. Mudasir, K. Karelius, N. H. Aprilita and E. T. Wahyuni, *J. Environ. Chem. Eng.*, 2016, **4**, 1839.

40 M. Bhaumik, T. Y. Leswifi, A. Maity, V. V. Srinivasu and M. S. Onyango, *J. Hazard. Mater.*, 2011, **186**, 150.

41 S. Schiewer and M. H. Wong, *Chemosphere*, 2000, **41**, 271.

42 K. Z. Setshedi, M. Bhaumik, M. S. Onyango and A. Maity, *Chem. Eng. J.*, 2015, **262**, 921.

43 C. M. Kede, P. P. Ndibewu, M. M. Kalumba, N. A. Panichev, H. M. Ngomo and J. M. Ketcha, *S. Afr. J. Chem.*, 2015, **68**, 226.

44 B. Henriques, G. Goncalves, N. Emami, E. Pereira, M. Vila and P. Marques, *J. Hazard. Mater.*, 2016, **301**, 453.

45 X. Peng, W. Zhang, L. Gai, H. Jiang, Y. Wang and L. Zhao, *Chem. Eng. J.*, 2015, **280**, 197.

46 Y. F. Guo, J. Deng, J. Y. Zhu, C. Zhou, C. Y. Zhou, X. J. Zhou and R. B. Bai, *RSC Adv.*, 2016, **6**, 39762.

47 S. B. Wu, L. T. Kong and J. H. Liu, *Res. Chem. Intermed.*, 2016, **42**, 4513.

48 X. Tao, K. Li, H. Yan, H. Yang and A. M. Li, *Environ. Pollut.*, 2016, **209**, 21.

49 O. S. Akintola, T. A. Saleh, M. M. Khaled and O. C. S. Al Hamouz, *J. Taiwan Inst. Chem. Eng.*, 2016, **60**, 602.

50 Y. F. Guo, Z. Wang, X. J. Zhou and R. B. Bai, *Res. Chem. Intermed.*, 2016, **10**, 1.

51 S. Nasirimoghaddam, S. Zeinali and S. Sabbaghi, *J. Ind. Eng. Chem.*, 2015, **27**, 79.

52 H. K. Moghaddam and M. Pakizeh, *J. Ind. Eng. Chem.*, 2015, **21**, 221.

53 B. Tawabini, S. Al-Khaldi, M. Atieh and M. Khaled, *Water Sci. Technol.*, 2010, **61**, 591.

54 K. Yaghmaeian, R. K. Mashizi, S. Nasseri, A. H. Mahvi, M. Alimohammadi and S. Nazmara, *J. Environ. Health Sci. Eng.*, 2015, **13**, 9.

55 D. K. Mondal, B. K. Nandi and M. K. Purkait, *J. Environ. Chem. Eng.*, 2013, **1**, 891.

56 V. Sangu, K. Kannan and K. Srinivasan, *Indian J. Chem. Technol.*, 2015, **22**, 219.

57 T. Takimoto, H. Tsue, R. Tamura and H. Sasaki, *Heterocycles*, 2015, **90**, 842.

58 F. H. Wang, W. Jiang, Y. Fang and C. W. Cheng, *Chem. Eng. J.*, 2015, **259**, 827.

59 J. C. Tang, H. H. Lv, Y. Y. Gong and Y. Huang, *Bioresour. Technol.*, 2015, **196**, 355.

60 Y. H. Duan, D. S. Han, B. Batchelor and A. Abdel-Wahab, *Colloids Surf., A*, 2016, **490**, 326.

61 Q. D. Qin, J. Ma and K. Liu, *J. Hazard. Mater.*, 2009, **162**, 133.